O2 Activation by Non-Heme Thiolate-Based Dinuclear Fe Complexes

Lianke Wang, Marcello Gennari, Fabián Cantú Reinhard, Sandeep Padamati, Christian Philouze, David Flot, Serhiy Demeshko, Wesley Browne, Franc Meyer, Sam de Visser, et al.

O_2 activation by non-heme thiolate-based dinuclear Fe complexes

Lianke Wang,[a,b] Marcello Gennari,[b,*] Fabián G. Cantú Reinhard,[c] Sandeep K. Padamati,[b,d] Christian Philouze,[b] David Flot,[e] Serhiy Demeshko,[f] Wesley Browne,[d] Franc Meyer,[f] Sam P. de Visser,[c,*] Carole Duboc[b,*]

[a] *Institutes of Physical Science and Information Technology, Anhui University, 230601, Hefei, Anhui, P. R. China*
[b] *Univ. Grenoble Alpes, CNRS UMR 5250, DCM, F-38000 Grenoble, France*
[c] *Manchester Institute of Biotechnology and Department of Chemical Engineering and Analytical Science, The University of Manchester, 131 Princess Street, Manchester M1 7DN, United Kingdom*
[d] *Molecular Inorganic Chemistry, Stratingh Institute for Chemistry, Faculty of Science and Engineering, University of Groningen, Nijenborgh 4, 9747AG, Groningen, The Netherlands*
[e] *ESRF European Synchrotron 71, Ave Martyrs Grenoble, Grenoble, France*
[f] *University of Göttingen, Institute of Inorganic Chemistry, Tammannstrasse 4, D- 37077 Göttingen, Germany*

***** corresponding authors: carole.duboc@univ-grenoble-alpes.fr; marcello.gennari@univ-grenoble-alpes.fr, sam.devisser@manchester.ac.uk

Abstract

Iron centers featuring thiolates in their metal coordination sphere (as ligands or substrates) are well known to activate dioxygen. Both heme and non-heme centers that contain iron-thiolate bonds are found in nature. Investigating the ability of iron-thiolate model complexes to activate O_2 is expected to improve the understanding of the key factors that direct reactivity to either iron or sulfur. We report here the structural and redox properties of a thiolate-based dinuclear Fe complex, $[Fe^{II}_2(LS)_2]$, (LS^{2-} = 2,2'-(2,2'-bipyridine-6,6'-iyl)bis(1,1-diphenylethanethiolate) and its reactivity with dioxygen, in comparison with its previously reported protonated counterpart, $[Fe^{II}_2(LS)(LSH)]^+$. When reaction with O_2 occurs in the absence of protons or in the presence of one equivalent of proton (i.e. from $[Fe^{II}_2(LS)(LSH)]^+$), unsupported μ-oxo or μ-hydroxo Fe^{III} dinuclear complexes ($[Fe^{III}_2(LS)_2O]$ and $[Fe^{III}_2(LS)_2(OH)]^+$, respectively) are generated. $[Fe^{III}_2(LS)_2O]$, reported previously but isolated here for the first time from O_2 activation, is characterized by single crystal X-ray diffraction and Mössbauer, Resonance Raman and NMR spectroscopies. The addition of protons leads to the release of water and the generation of a mixture of two Fe-based "oxygen-free" species. DFT-calculations provide insight into the formation of the μ-oxo or μ-hydroxo Fe^{III} dimers, predicting that a dinuclear μ-peroxo Fe^{III} intermediate is key to

reactivity, and the structure of which changes as a function of protonation state. Compared to previously reported Mn-thiolate analogues, the evolution of the peroxo intermediates to the final products is different and involves a comproportionation vs a dismutation process for the Mn and Fe derivate, respectively.

Introduction

Iron centers play a key role in dioxygen binding and activation, in both enzymes and synthetic complexes.[1-5] Apart from the most classical N- and O- based donor ligands, a subclass of iron centers that activate O_2 features thiolates in the metal coordination sphere, whether as supporting ligands or as substrates. In nature, Fe-S(cysteinate) bonds are found in the heme centers present in cytochromes P450,[6-7] which enable monoxygenation of inert C-H bonds. The structurally analogous nitric oxide synthase[8] releases the cellular signalling molecule nitric oxide (NO) through a reaction of dioxygen with L-arginine on a heme center. Regarding biological non-heme Fe centers, several enzymes are able to carry out reactions between O_2 and thiolate-based substrates through Fe-S bond formation. These include thiol oxygenases, among which the cysteine dioxygenase[9-15] responsible for the oxidation of cysteine to cysteine sulfinic acid, and the isopenicillin N synthase,[16] which enables the oxidation of the thiolate-containing tripeptide δ-(L-α-aminoadipoyl)-L-cysteinyl-D-valine to form isopenicillin N. In addition to the reactivity of these two families of Fe-based metalloenzymes, the coordination mode of the thiolate to the metal center is also different: in non-heme systems, the thiolate binds in the *cis* position with respect to the O_2 coordination site,[17] while in heme centers it binds in the axial position, *trans* to the O_2 binding site.

In this context, chemists have developed a broad range of synthetic non-heme iron-thiolate model complexes. They can be distinguished in three main classes based on their reactivity with dioxygen: (i) those leading to the production of S-oxygenated species, such as sulfenic, sulfinic and sulfonic acid derivatives;[17-24] (ii) those promoting sulfur oxidation to generate disulfide;[25-27] and (iii) those forming iron-oxygen adducts, in which the thiolate ligand remains unmodified. The last case includes, mono- or dinuclear Fe^{II}-thiolate precursors that invariably generate unsupported μ-oxo bridged Fe^{III} dimers in the presence of O_2.[28-30]

Efforts continue to expand the library of O_2-reactive Fe-thiolate complexes in view of preferentially directing the reactivity to iron or sulfur, and in the last case to control the selectivity, i.e. sulfoxygenation vs disulfide formation. Such objective requires the complete understanding of the various reaction mechanisms and the identification of the key factors, in

terms of ligand design, metal spin state, and position of the metal-bound thiolate with respect to the O_2 activation site.

We recently reported a study on a dinuclear Fe^{II}-thiolate complex, $[Fe^{II}_2(LS)(LSH)]BF_4$ (**$[Fe_2^{SH}]^+$**, LS^{2-} = 2,2'-(2,2'-bipyridine-6,6'-iyl)bis(1,1-diphenylethanethiolate, Scheme 1), active for proton-assisted O_2 reduction catalysis, whose selectivity varies as a function of the experimental conditions. Hydrogen peroxide is the main product in the presence of a chemical reducing agent, whereas water is the major product under electrochemical conditions.[31] The peculiarity of this complex is the presence of an unusual metal-bound thiol group, proposed to be involved in proton relay during catalysis and to be responsible for the reaction bifurcation.

In the present work, we describe the reactivity with dioxygen of the **$[Fe_2^{SH}]^+$** complex in the absence of additional protons, and of the parent deprotonated complex $[Fe^{II}_2(LS)_2]$ (**$[Fe_2^{S}]$**). We investigate the mechanism of the O_2 activation process and evaluate the role of the metal-bound thiol present only in **$[Fe_2^{SH}]^+$**. The full characterization of **$[Fe_2^{S}]$** is also reported together with its redox properties. The electrochemical oxidation of both dimercapto-bridged Fe^{II} complexes results in the oxidation of both sulfur and metal with the formation of two previously reported complexes in equilibrium:[32] the disulfide complex $[Fe^{II}_2(LSSL)]^{2+}$, **$[Fe_2^{SS}]^{2+}$**, $(LSSL)^{2-}$ = disulfide form of the LS^{2-} ligand) and the complex $[Fe^{III}(LS)(MeCN)]^+$ (**$[Fe^{MeCN}]^+$**). Remarkably, in the presence of O_2, the iron-bound thiolates of **$[Fe_2^{SH}]^+$** and **$[Fe_2^{S}]$** are unreactive towards O_2. However, the iron(II) ions react with O_2 by an inner sphere mechanism, affording rare examples of thiolate-ligated unsupported μ-oxo and μ-hydroxo bridged Fe^{III} dimers ($[Fe^{III}_2(LS)_2O]$, **$[Fe_2^{O}]$**, and $[Fe^{III}_2(LS)_2(OH)]^+$, **$[Fe_2^{OH}]^+$**, starting from **$[Fe_2^{S}]$** and **$[Fe_2^{SH}]^+$**, respectively, see Schemes 1 and 2). Finally, through DFT-calculations we have investigated the O_2 activation mechanism of **$[Fe_2^{S}]$** and compared the structure, thermodynamics and mechanistic scenarios with those reported for the protonated counterpart **$[Fe_2^{SH}]^+$**, as well as the previously reported analogous Mn^{II} complexes.[33-34]

Results

Synthesis and crystal structure of the Fe^{II}-thiolate dimer [Fe_2^{S}]. The previously reported dimercapto-bridged Fe^{II} dinuclear complex $[Fe^{II}_2(LS)(LSH)]BF_4$ (**$[Fe_2^{SH}]^+$**) displayed an unusual metal-bound thiol. This complex was obtained by reacting the LS^{2-} ligand[35] with $Fe(BF_4)_2{\cdot}6H_2O$ (1.2 equiv.) in THF under inert atmosphere.[36] In the present work, **$[Fe_2^{SH}]^+$** was deprotonated to afford the dimercapto-bridged Fe^{II} dimer $[Fe^{II}_2(LS)_2]$ (**$[Fe_2^{S}]$**) in the presence of NaH in MeCN.

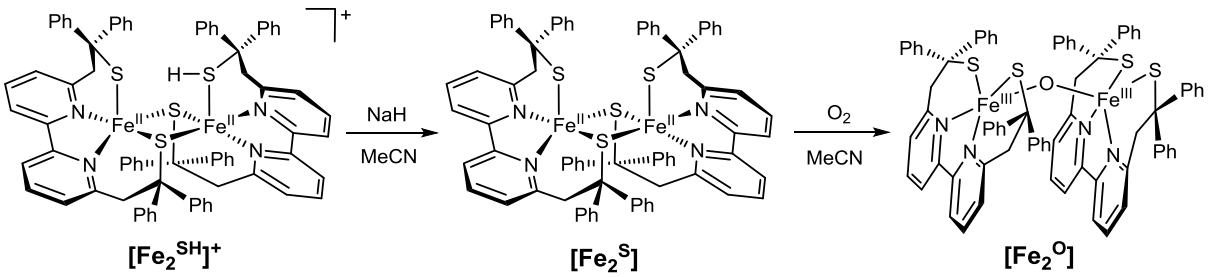

Scheme 1. Synthesis of **[Fe$_2^{S}$]** and **[Fe$_2^{O}$]**.

The single-crystal X-ray diffraction structure of **[Fe$_2^{S}$]**, shown in Figures 1 and S1 (crystallographic data with bond distances and angles in Tables S1 and S2 of the Supporting Information, respectively), displays two crystallographically independent, but chemically identical, [Fe$^{II}_2$(LS)$_2$] dimers. Both units (A and B) display a quasi-planar [28] diamond core as observed (deviations from the S2Fe1AS3Fe2A and S2Fe1BS3Fe2B planes are less than 0.2 and 0.1 Å, respectively). The two iron sites are not equivalent, each Fe^{II} center being pentacoordinated and surrounded by an N2S3 donor set in a distorted square pyramidal geometry (τ_5 = 0.44 for Fe1A / τ_5 = 0.44 for Fe2A and τ_5 = 0.46 for Fe1B / τ_5 = 0.43 for Fe2B).[37] In each dimeric unit, the two Fe-S$_{terminal}$ distances are comparable (*e.g.* Fe1A-S1A = 2.3382(15) Å and Fe2A-S4A = 2.3632(17) Å), in agreement with the presence of two terminally bound thiolates, and in contrast to what is observed in **[Fe$_2^{SH}$]$^+$** (Fe1−S1 = 2.3566(11) Å and Fe2−S4(thiol) = 2.5387(11) Å).[36] The loss of the intramolecular S-H···S hydrogen-bond interaction present in **[Fe$_2^{SH}$]$^+$** leads to a slight increase of the Fe···Fe distance (3.2179(13) and 3.2544(12) Å for the two crystallographically independent molecules vs 3.1107(7) Å in **[Fe$_2^{SH}$]$^+$**), as well as an increase of the S…S distance (5.060 and 4.816 Å for the two crystallographically independent molecules of **[Fe$_2^{S}$]** vs 3.594 Å in **[Fe$_2^{SH}$]$^+$**).

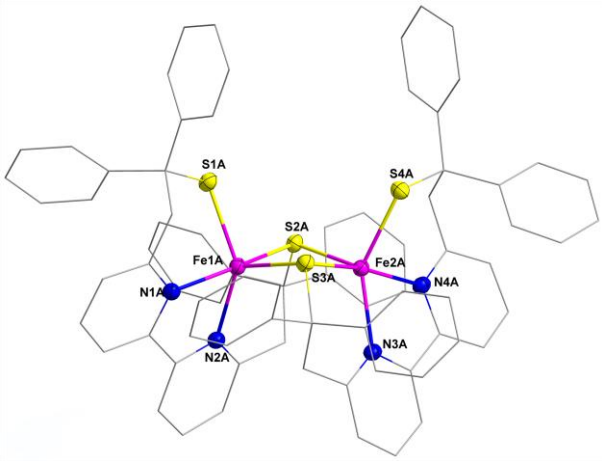

Figure 1. Molecular structure of **[Fe$_2^S$]**·0.5CH_3CN·0.75Et_2O determined by X-ray diffraction. The thermal ellipsoids of the metal cores are drawn at 30% probability level. All hydrogen atoms and solvent molecules are omitted for clarity.

Redox properties of [Fe$_2^S$]. The signal at 1291.2 *m/z* in the electrospray ionization mass (ESI-MS) spectrum of an acetonitrile solution of **[Fe$_2^S$]** is assigned to the sodium adduct of [$Fe^{II}_2(LS)_2$] (Figure S2, Supporting Information), and suggests that **[Fe$_2^S$]** mostly remains dinuclear in solution. The cyclic voltammogram (CV, see Figure 2) of **[Fe$_2^S$]** shows a quasi-reversible oxidation at $E_{1/2}$ = -0.58 V vs Fc^+/Fc (ΔE_p = 110 mV). Bulk electrolysis at -0.50 V of an acetonitrile solution of **[Fe$_2^S$]** (corresponding to an exchange of approximately one electron per iron atom) results in a mixture of two species, i.e. the mononuclear $[Fe^{III}(LS)(MeCN)]^+$ (**[Fe^{MeCN}]$^+$**) and the dinuclear $[Fe^{II}_2(LSSL)]^{2+}$ (**[Fe$_2^{SS}$]$^{2+}$**), $(LSSL)^{2-}$ = disulfide form of the LS^{2-} ligand), in a 2:1 ratio. The same mixture, called **Fe^{ox}** for the sake of simplicity, was previously generated by electrochemical oxidation of the protonated complex, **[Fe$_2^{SH}$]$^+$**, and its physical properties were investigated earlier.[36]

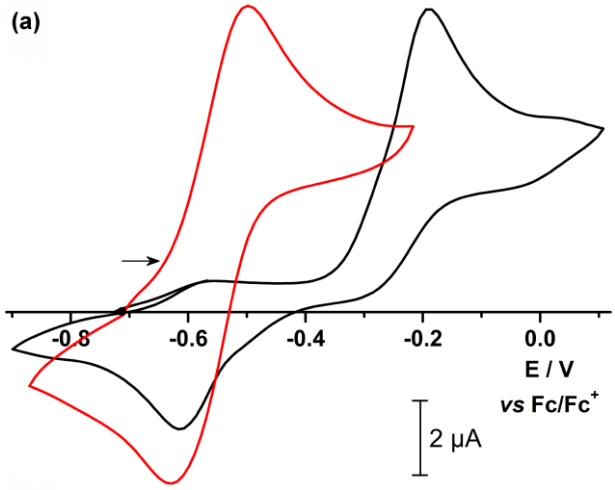

Figure 2. CVs of 0.5 mM solutions (MeCN, 0.1 M Bu_4NClO_4) of **[Fe$_2^S$]** (red line) and **[Fe$_2^{SH}$]$^+$** (black line). GC working electrode, 100 $mV{\cdot}s^{-1}$.

Comparing the CVs of **[Fe$_2^S$]** with those of **[Fe$_2^{SH}$]$^+$**, leads to the conclusion that protonation of **[Fe$_2^S$]** induces notable redox changes. More specifically, the oxidation becomes irreversible after protonation of the dimer, with a 330 mV positive shift in E_{pa} compared to that of **[Fe$_2^S$]** (-0.19 V and -0.52 V, respectively). A similar shift of 300 mV was observed for the parent Mn-based complexes (**[Mn$_2^S$]** and **[Mn^{SH}]$^+$**). The substitution of Mn for Fe in **[M$_2^S$]** induces a shift of about -130 mV for the "M_2^{II}/M_2^{III}" redox process ($E_{1/2}$ = -0.58 V for Fe vs $E_{1/2}$ = -0.45 V for Mn),[33] similar to that observed between the **[Mn$_2^{SH}$]$^+$** and **[Fe$_2^{SH}$]$^+$** complexes.

Reaction of $[Fe_2^{S(H)}]^{0/+}$ with O_2.

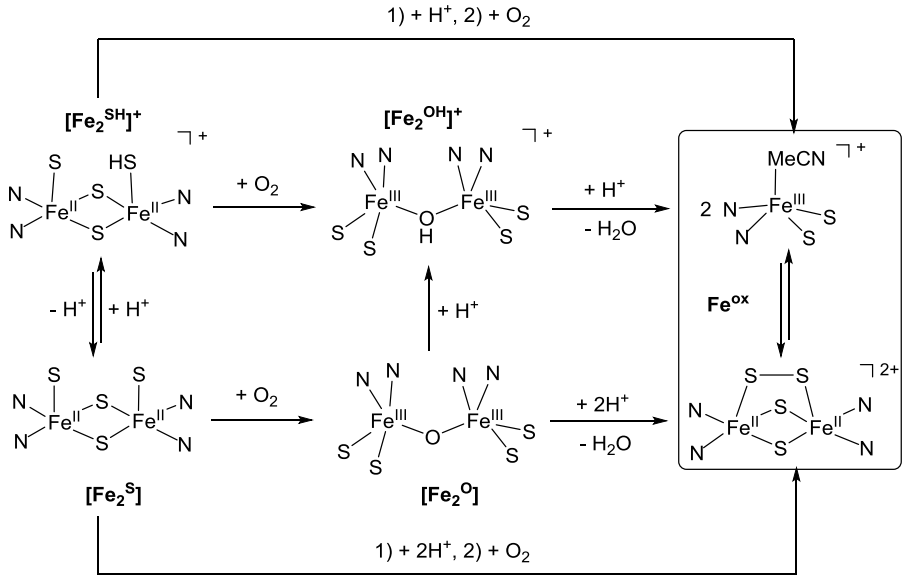

Scheme 2. Dioxygen reactivity of the Fe-thiolate complexes discussed depends on the presence of protons (simplified representation).

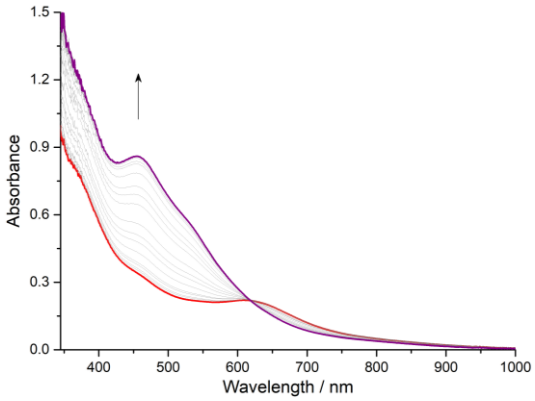

Figure 3. UV-vis absorption spectrum of **$[Fe_2^S]$** (0.1 mM, 1 cm path length, scan every 0.5 s) in acetonitrile before (red) and over time after (to violet) injection of O_2.

The reactivity of the **$[Fe_2^S]$** and **$[Fe_2^{SH}]^+$** complexes with dioxygen, in the absence or presence of protons (2,6-lutidinium, $LutH^+$), is summarized in Scheme 2. When a dilute (~0.1 mM) green solution of **$[Fe_2^S]$** in acetonitrile is exposed to air or O_2 at room temperature, the color changes rapidly to brown. The UV-vis absorption spectrum of the final product displays a transition at 455 nm ($\varepsilon \approx 8600\ M^{-1}\cdot cm^{-1}$), that can be assigned to a thiolate → Fe^{III} charge transfer band,[32, 38] and a shoulder at 535 nm (Figure 3). The ^1H NMR spectrum at 298 K identifies two characteristic paramagnetically-shifted signals at 14.65 and 21.11 ppm (Figure

4). Based on these features, the iron-oxygen species generated has been assigned as the μ-oxo bridged Fe^{III} dimer [$(Fe^{III}_2(LS)_2O$] (**[Fe_2^O]**). Indeed, this structure has been proposed previously as the product of the reaction of the chloride adduct [Fe^{III}(LS)Cl] with Bu_4NOH.[35] In this latter report the assignment was based on UV-vis absorption and NMR spectroscopic data alone. Here, the presence of an isosbestic point at 617 nm (see Figure 3) is consistent with the direct conversion from **[Fe_2^S]** to **[Fe_2^O]** without detectable intermediates (i.e. intermediates were not detected even when the experiments are carried out at low temperature up to -40°C).

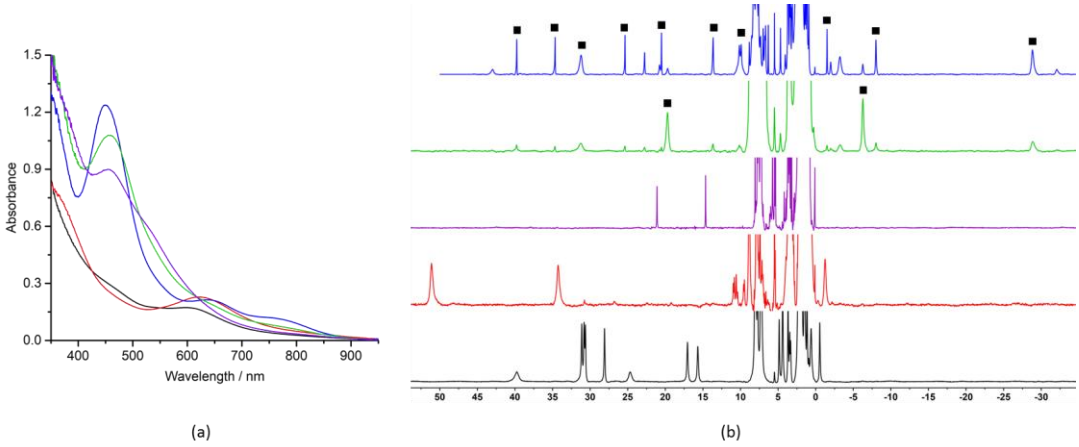

Figure 4. (a) UV-vis spectra (0.1 mM, 1 cm path length) and (b) ^{1}H NMR (500 MHz) spectra of **[Fe_2^{SH}]$^+$** (black), **[Fe_2^S]** (red), **[Fe_2^O]** (violet), **[Fe_2^{OH}]$^+$** (green) and **Fe^{ox}** (blue) in CH_3CN/CD_3CN (■ indicates the main species).

Here, we were able to isolate **[Fe_2^O]** from the reaction between **[Fe_2^S]** and O_2 in good yield (81%) and to resolve its structure by single crystal X-ray diffraction (Figure 5a), confirming the previous assignment. In the structure, both Fe centers are pentacoordinated and surrounded by an N_2S_2O donor set in two distinct geometries, i.e. in distorted square-pyramidal (τ_5 = 0.33 for Fe1) and trigonal bipyramidal (τ_5 = 0.59 for Fe2) environments.[37] The Fe-O distances (Fe1-O1 = 1.780(7) Å, Fe2-O1 = 1.803(8) Å) and Fe1-O1-Fe2 angle (145.1(5)°) are in the reported ranges for μ–oxo di-Fe^{III} complexes. The zero-field powder Mössbauer spectrum recorded at 80 K (Figure 5b) displays a single doublet (δ = 0.42 mm·s^{-1} and ΔE_Q = 1.22 mm·s^{-1}) typical of high-spin (S = 5/2) Fe^{III} ions.

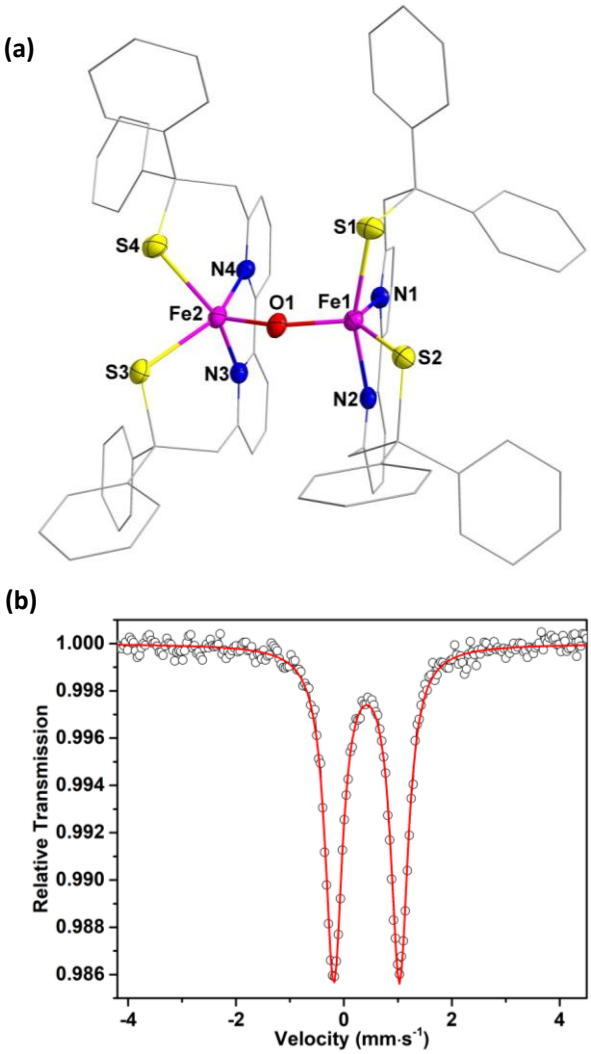

Figure 5. Solid state characterization of **[Fe_2^O]**: (a) Molecular structure (thermal ellipsoids of the metal core drawn at 10% probability level, hydrogen atoms omitted for clarity); (b) zero-field Mössbauer spectrum (80 K).

ESI-MS spectrometry and Raman spectroscopy with $^{16}O_2$ and $^{18}O_2$ were carried out to identify the origin of the oxygen atom. The ESI-MS spectrum of **[Fe_2^O]** (generated in situ in MeCN) shows a signal at 1323.2 *m*/*z*, corresponding to the potassium adduct of [$(Fe_2(LS)_2O$] (Figure 6a). When the complex is synthesized from $^{18}O_2$, the corresponding ^{18}O-labeled compound is observed in the ESI-MS spectrum with the expected shift of +2, thus demonstrating that a single oxygen atom of O_2 is incorporated into the complex and that the μ-oxo bridge derives from dioxygen. Consistent with these data, the powder Raman spectrum of **[Fe_2^O]** (λ_{exc} = 633 nm, Figure 6b) shows a band at 804 cm^{-1} that downshifts to 771 cm^{-1} for the ^{18}O-labeled compound, i.e. an isotopic shift of $\Delta\nu$ = 33 cm^{-1}. This band can be assigned to an Fe-O-Fe stretch vibration,[39] based on the isotopic shift ($\Delta\nu$ = 37 cm^{-1} using a two atom

approximation) and on previously reported data on μ-oxo-bridged diiron complexes. The DFT-calculated vibrational frequencies of the **[Fe_2^O]** complex match those obtained from experiment well, namely 813 cm^{-1} was predicted for the vibration due to the Fe-^{16}O-Fe stretching mode, see Supporting Information).

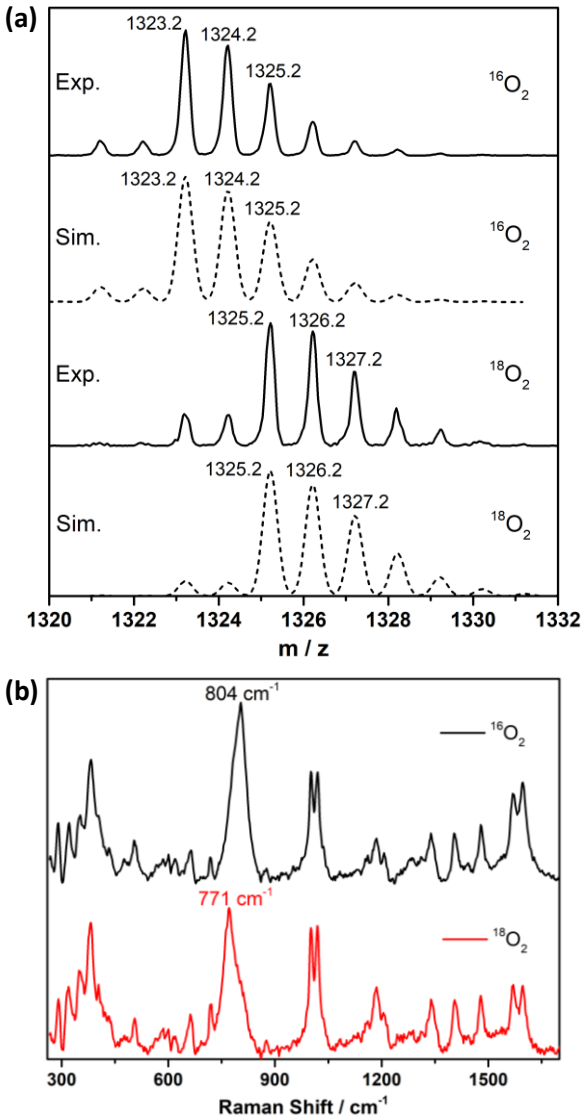

Figure 6. Experimental and simulated (a) ESI-MS ([$(Fe_2(LS)_2OK]^+$ peak, MeCN), and (b) Raman spectra of **[Fe_2^O]** generated from **[Fe_2^S]** and either $^{16}O_2$ or $^{18}O_2$.

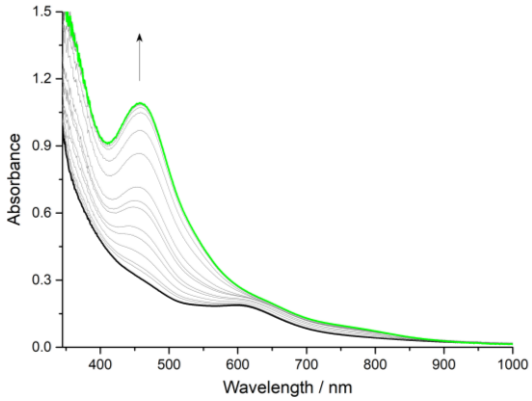

Figure 7. UV-vis absorption spectra of $\mathbf{[Fe_2^{SH}]^+}$ (0.1 mM, 1 cm path length, scan every 1 s) in MeCN before (black) and after (green) injection of O_2.

Addition of air to the thiol-containing $\mathbf{[Fe_2^{SH}]^+}$ complex in acetonitrile leads to the formation of a new stable species observed by UV-vis absorption spectroscopy (Figure 7). The ESI-MS spectrum of the generated product displays a single peak at 1285.3 *m*/*z* (Supporting Information, Figure S2) corresponding to the protonated form of $\mathbf{[Fe_2^{O}]}$. Coherently, the UV-vis and ^{1}H NMR spectra of this monoxygenated adduct (see Figure 4) match those obtained by addition of one equiv. of $LutH^+$ to $\mathbf{[Fe_2^{O}]}$ (Figure 8). These experiments demonstrate that the reaction of $\mathbf{[Fe_2^{SH}]^+}$ with O_2 affords the protonated form of $\mathbf{[Fe_2^{O}]}$. DFT calculations propose it to be on the bridging oxygen atom (resulting in a hydroxo-bridged complex $[(Fe^{III}{}_2(LS)_2(OH)]^+$, i.e. $\mathbf{[Fe_2^{OH}]^+}$) rather than on the thiolate. The UV-vis absorption spectrum of $\mathbf{[Fe_2^{OH}]^+}$ differs from that of $\mathbf{[Fe_2^{O}]}$, with only one thiolate → Fe^{III} CT transition (at 458 nm, ε ≈ 10800 $M^{-1}\cdot cm^{-1}$) and the paramagnetically shifted signals in the ^{1}H NMR spectrum between -6.26 and 19.69 ppm (Figure 4).

While both $\mathbf{[Fe_2^{O}]}$ and $\mathbf{[Fe_2^{OH}]^+}$ are stable in acetonitrile in the absence of protons, they react instantaneously with $LutH^+$. Indeed, the addition of 2 and 1 equiv. of $LutH^+$ to acetonitrile solutions of $\mathbf{[Fe_2^{O}]}$ and $\mathbf{[Fe_2^{OH}]^+}$, respectively, leads to the quantitative formation of $\mathbf{Fe^{ox}}$ as indicated by the presence of two isosbestic points: one at 486 nm for the conversion of $\mathbf{[Fe_2^{O}]}$ into $\mathbf{[Fe_2^{OH}]^+}$ and the second at 502 nm for the conversion of $\mathbf{[Fe_2^{OH}]^+}$ into $\mathbf{Fe^{ox}}$ (Figure 8).[32] The same speciation behavior is observed when the addition of proton(s) occurs before exposing $\mathbf{[Fe_2^{S(H)}]^{0/+}}$ to dioxygen (Figure S6). The conversion of $\mathbf{[Fe_2^{O}]}$ into $\mathbf{Fe^{ox}}$ occurs through two well-separated steps, corresponding to the successive additions of one proton as indicated by the overall NMR and UV-vis data.

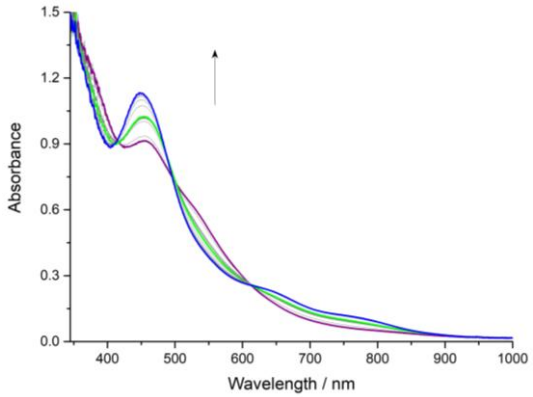

Figure 8. UV-vis spectra of **[Fe_2^O]** (generated from 0.1 mM **[Fe_2^S]** with O_2 in MeCN, 1 cm path length, scan every 1 s) in MeCN before (violet) and after addition of 1 (green) and 2 (blue) equivalent(s) of $LutH^+$.

Mechanistic investigation.

Density functional theory (DFT) calculations were then performed to gain insight into the mechanistic details of the O_2 activation processes by **[Fe_2^S]** and **[Fe_2^{SH}]$^+$**. Individual structures along the proposed mechanism (Schemes 3-5) were calculated for the reaction initiated with **[Fe_2^S]** using two different models that differ from their size but give comparable results. Only thermodynamic data obtained with the larger model are discussed in the text.

The **[Fe_2^S]** optimized geometry matches the crystallographically determined structure shown in Figure 1 well with similar Fe-$S_{terminal}$ distances of 2.381/2.372 Å. In the computational structure, the two iron centers are slightly further apart than seen in the crystal (3.469 Å calculated *versus* 3.2179(13)-3.2544(12) Å in the crystal), which is probably due to the fact that the calculations were run in the gas-phase. Changing the density functional from B3LYP to BLYP gives little change to the Fe-Fe distance (3.454 Å) and therefore, the calculations show little sensitivity to the choice of the density functional method.

The paradigm mechanism for dioxygen activation by diiron complexes implies the coordination of O_2 to one of the metal sites to afford a superoxo intermediate.[1] In the case of **[Fe_2^S]**, DFT calculations predict the formation of a dinuclear $Fe^{II}Fe^{III}$-superoxo species, **[$Fe_2^{OO\bullet}$]**, with the superoxo terminally bound to one Fe ion (see Scheme 3). The strongly endergonic character of this step (ΔG = +27.3 kcal·mol^{-1}) is comparable with the first O_2-activation step for the protonated form of the complex, **[Fe_2^{SH}]$^+$** (ΔG = +21.0 kcal·mol^{-1}).

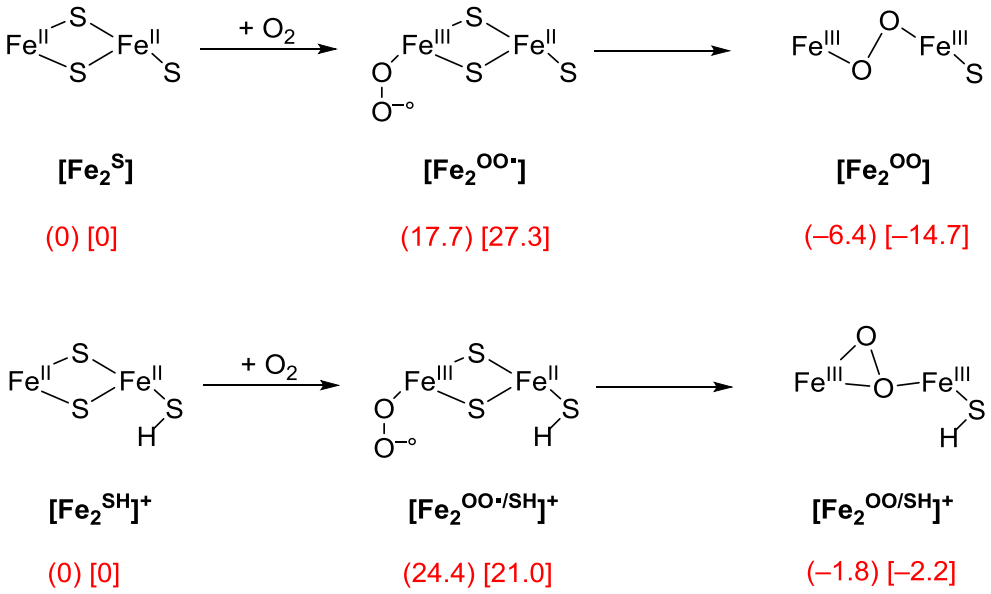

Scheme 3. First steps of the dioxygen activation process with **[Fe$_2^{S}$]** (above) and **[Fe$_2^{SH}$]$^+$** (below) predicted by DFT calculations. Energies in red are in kcal·mol^{-1} relative to **[Fe$_2^{S}$]** + O_2 (or **[Fe$_2^{SH}$]$^+$** + O_2) for the (small) and [large] models and are calculated at UB3LYP/BS2//UB3LYP/BS1+ZPC level in Gaussian.

Subsequently, **[Fe$_2^{OO•}$]** evolves into a *trans*-μ-1,2-peroxo diiron(III) complex, **[Fe$_2^{OO}$]** (see Scheme 3). The highly exergonic character of the second step for the formation of the **[Fe$_2^{OO}$]** intermediate (-14.7 kcal·mol^{-1} *vs* only -2.2 kcal·mol^{-1} for the formation of the protonated counterpart **[Fe$_2^{OO/SH}$]$^+$**) is proposed to drive the entire reaction process, and thus should overcome the thermodynamically uphill first step. The most stable structure of the peroxo complex consists of an unsupported *trans*-μ-1,2 peroxo dinuclear Fe^{III} unit. It notably differs from the structure calculated for the reaction of **[Fe$_2^{SH}$]$^+$** with O_2 (see Scheme 3):[36] **[Fe$_2^{OO/SH}$]$^+$** was found to be less symmetric, with a rare μ, η^1:η^2-peroxo coordination mode. The protonation state of the iron-peroxo intermediate has thus an important effect on its structure, with a potential impact on its reactivity. Unsupported peroxo dinuclear Fe^{III} complexes have been characterized only with heme subunits.[40] In the case of non-heme dinuclear Fe^{III} peroxo complexes, they exclusively display the *cis*-μ-1,2 coordination mode in the presence of one or more additional bridges (e.g. carboxylate, phenolato) to stabilize such species.[41-43] However, the generation of dinuclear *trans*-μ-1,2 peroxo Fe^{III} complexes from O_2 and non-heme Fe^{II} complexes is largely admitted.[3, 36] Such unsupported peroxo species with a *trans*-μ-1,2 coordination mode has been recently isolated and fully characterized from the

reaction of a mononuclear Mn^{II}-thiolate complex with O_2,[44] demonstrating that the presence of thiolates can help in the stabilization of such species.

We then considered the generation of the μ-oxo bridged Fe dimer **[Fe_2^{O}]** from the μ-peroxo bridged Fe dimer **[Fe_2^{OO}]**, for which two possible mechanistic scenarios were tested (Scheme 4):[40, 45] (i) the dismutation of two **[Fe_2^{OO}]** complexes to afford two molecules of **[Fe_2^{O}]** and O_2 (pathway A), and (ii) the reaction between **[Fe_2^{OO}]** and the initial reactant **[Fe_2^{S}]** to afford two molecules of **[Fe_2^{O}]** through a comproportionation process (pathway B). Both pathways are strongly exergonic with close values of -91.0 and -84.0 kcal mol^{-1}, respectively, precluding conclusions being drawn as to the preferred pathway.

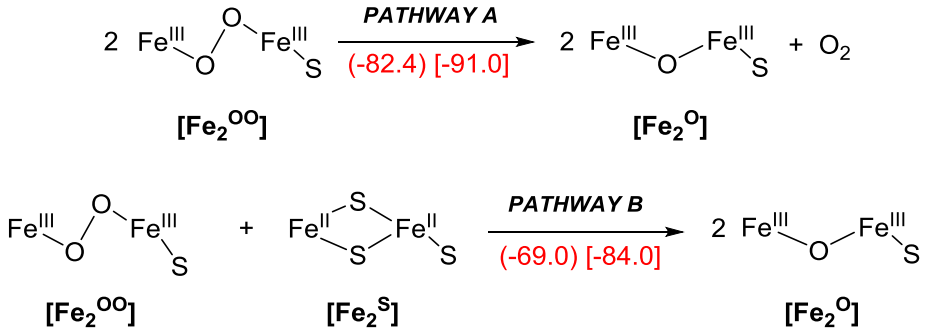

Scheme 4 Two possible reaction pathways for the conversion of **[Fe_2^{OO}]** to **[Fe_2^{O}]** either as a dismutation reaction (top) or as a comproportionation process with the reactant (bottom). Reaction free energies (ΔG^0, kcal·mol^{-1}) have been calculated using DFT at the BLYP/BS2//BLYP/BS1 level of theory for the (small) and [large] models.

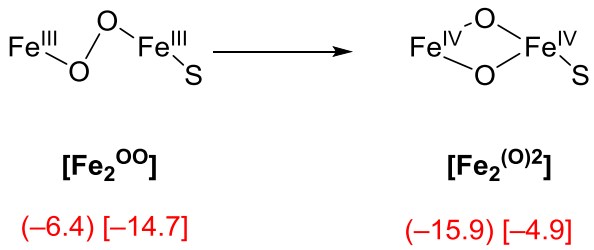

Scheme 5. Breaking of the O-O bond in **[Fe_2^{OO}]** is predicted to afford the **[$Fe_2^{(O)2}$]** intermediate. Energies in red are in kcal·mol^{-1} relative to **[Fe_2^{S}]** + O_2 for the (small) and [large] models and are calculated at UB3LYP/BS2//UB3LYP/BS1+ZPC in Gaussian.

For both pathways, the cleavage of the O-O bond of **[Fe_2^{OO}]** is required. When calculating the evolution of the peroxo **[Fe_2^{OO}]** intermediate via O-O rupture, the exergonic formation of a bis μ-oxo bridged Fe^{IV} dimer, **[$Fe_2^{(O)2}$]** is predicted (Scheme 5). This type of species is definitively accepted in the literature with a number of such highly active intermediates fully characterized in different environments.[46] In the case of the isostructural Mn-thiolate

complex,[33] the corresponding bis μ-oxo bridged Mn^{IV} dimer (**[$Mn_2^{(O)2}$]**) was stable enough to be isolated and fully characterized. It was shown experimentally that the dinuclear μ-oxo Mn^{III} complex forms through comproportionation. Indeed, depending on the experimental conditions (temperature, relative concentrations between the complex and O_2), either the dinuclear di-μ-oxo Mn^{IV} complex or the dinuclear μ-oxo Mn^{III} complex is generated. In the case of the Fe system, we were unable to trap and characterize the dinuclear di-μ-oxo Fe^{IV} complex, **[$Fe_2^{(O)2}$]**, despite many attempts. We thus propose that **[Fe_2^{O}]** is more likely generated through the dismutation pathway (Scheme 4, pathway A). Similarly, we also did not succeed in observing the protonated form of the bis μ-oxo Fe^{IV} complex, i.e. **[$Fe_2^{(O)2/SH}$]$^+$**.[36] Consequently we propose that a dismutation process also occurs between two protonated peroxo complexes (**[$Fe_2^{OO/SH}$]$^+$**) to generate **[Fe_2^{OH}]$^+$**.

Concluding remarks

In this work, we report the inner-sphere reactivity of the thiolate-based dinuclear Fe complex, $[Fe^{II}_2(LS)_2]$, with O_2. Depending on the number of proton equivalents, the final Fe-based product varies. When the reaction occurs in the absence of protons or in the presence of one equivalent of proton, an unsupported μ-oxo or μ-hydroxo Fe^{III} dinuclear complex is isolated, respectively. The addition of a second proton leads to the generation of a mixture of "oxygen-free" complexes, i.e. a disulfide Fe^{II} dinuclear complex and a thiolate Fe^{III} mononuclear complex, with the concomitant release of a water molecule. In no case, however, cysteine oxygenase activity with sulfur oxygenation has been observed.

The detection of a μ-hydroxo Fe^{III} dinuclear complex is not trivial, since it is known that the acidity of a bridging hydroxide increases with the iron oxidation state.[47] For example, protonation of the thiolate-containing μ-oxo Fe^{III} dimer reported by the group of Kovacs[29] leads to the direct release of water, without transient formation of a μ-hydroxo Fe^{III} dimer.

Regarding the O_2 activation pathway, DFT calculations predict a similar process for the fully deprotonated $[Fe^{II}_2(LS)_2]$ and the thiol-containing $[Fe^{II}_2(LS)(LSH)]^+$ complexes. The main difference arises from the structure of the Fe^{III}-peroxo intermediate, the presence of the thiol inducing a loss of symmetry in the Fe_2O_2 moiety. Interestingly this process is different from that proposed for the analogous manganese complexes.[33] While for Mn the mechanism includes a comproportionation step involving the starting complex and a Mn^{IV} bis μ-oxo adduct, in the Fe system the final product is predicted to be generated by dismutation of two Fe^{III}-peroxo complexes.

As found in the active site of enzymes that activate O_2 with a non-heme Fe center, in the present system, the O_2 binding site is in *cis* position with respect to a thiolate ligand. While such enzymes are involved in the oxygenation of the metal-bound thiolate, here such reactivity is not observed. It can thus be concluded that the binding mode of O_2 with respect to the thiolate position can be not strictly correlated to S-centered reactivity.

Experimental section

General. **[Fe_2^{SH}]**BF_4 was synthesized as previously reported,[36] all other reagents were used as received. Acetonitrile was distilled over CaH_2 and degassed prior to use. The synthesis and isolation of **[Fe_2^S]** was carried out under argon (in a glove box with less than 5 ppm of O_2). The infrared spectra were recorded on a Thermo Scientific Nicolet iS10 FT-IR spectrometer (equipped with ATR accessory) as neat solids. ^{1}H NMR spectra were recorded on Bruker Avance III 500 MHz spectrometers. The elemental analyses were carried out with a C, H, N analyzer (SCA, CNRS). The ESI-MS spectra were registered on a Bruker Esquire 3000 Plus or Amazon speed ion trap spectrometer equipped with an electrospray ion source (ESI). The samples were analyzed in positive ionization mode by direct perfusion in the ESI-MS interface (ESI capillary voltage= 2kV, sampling cone voltage= 40 V). The electronic absorption spectra were recorded on a ZEISS MC5601 absorption spectrophotometer in quartz cells (optical path length: 1 cm).

Synthesis of $[Fe^{II}(LS)]_2$ *(****[Fe_2^S]****).* Solid NaH (60% in mineral oil, 8.0 mg, 0.200 mmol) was suspended in MeCN (8 mL) at 293 K and the powder of **[Fe_2^{SH}]**BF_4 (28.0 mg, 0.020 mmol) was added under stirring. The color of the reaction mixture turned from brown to green with time. After 10 min, the excess NaH was filtered off. X-ray suitable dark-green crystals of **[Fe_2^S]**·0.5CH_3CN·0.75Et_2O (14 mg, 0.010 mmol, 57%) were obtained by slow diffusion of diethyl ether into the green filtrate at 293 K. ESI-MS (CH_3CN, *m/z*,): 1291.2, $[Fe_2(LS)_2Na]^+$. ^{1}H NMR (CD_3CN, 500 MHz): δ 51.10, 34.25, -1.25.

Synthesis of $[(Fe^{III}{}_2(LS)_2O]$ **(*[Fe_2^O]*).** Dry dioxygen (3 mL, 1 atm) was injected into a green solution of **[Fe_2^S]**, prepared as described above (starting from the same amounts of reactants and directly used before the crystallization step), under stirring. The solution turned from green to brown and a brown precipitate was formed after few min. After 10 min, the precipitate was separated by filtration, washed with CH_3CN (5 mL), dried and collected as a

brown powder (**[Fe_2^O]**, 15.3 mg, 0.012 mmol, 58%). Anal. Calcd. for $C_{76}H_{60}N_4S_4Fe_2O{\cdot}0.2MeCN{\cdot}4.2H_2O$: C, 67.02; H, 5.08; N, 4.30; Found: C, 66.97; H, 4.99; N, 4.33. IR (cm^{-1}): 1599 (s), 1571 (m), 1488 (s), 1469 (m), 1442 (s), 1314 (vw), 1271 (w), 1184 (w), 1159 (vw), 1083 (s), 1026 (m), 808 (w), 791 (vw), 746 (s), 696 (vs), 666 (m), 651 (m), 622 (m), 600 (m), 585 (w). ESI-MS (CH_3CN, *m/z*): 1307.2, $[Fe_2(LS)_2ONa]^+$, 1323.2, $[Fe_2(LS)_2OK]^+$. ^1H NMR (CD_3CN, 500 MHz): δ 21.11, 14.65. X-ray suitable black single crystals of **[Fe_2^O]** were obtained by slow diffusion of diethyl ether into a solution of the product in DMF : MeCN (1:1) at 293 K.

X-ray Crystallography. Single-crystal diffraction data for **[Fe_2^S]**$\cdot 0.5CH_3CN \cdot 0.75Et_2O$ were measured on an Nonius-Bruker 4 circles diffractometer with a APEXII CCD detector and an Incoatec high brilliance microsource with multilayer mirrors to monochromatize the MoKα radiation (λ = 0.71073Å) at 200 K. Eval, Sadabs and Xprep (Nonius-Bruker) were used for cell refinements, integration, absorption correction and data reduction. Single-crystal diffraction data for **[Fe_2^O]** were collected at beamline Gemini1[48] of the ESRF synchrotron (Grenoble, France) using a Dectris Pilatus 6M detector and a Maatel 2 circles Mini-diffractometer at 100 K with a toroidal Si 111 mirror monochromator at λ = 0.7293 Å. Integration, of the data were performed using XDS Package.[49] Absorption correction and scaling was performed with Sadabs and Xprep. Subsequent steps were run under Olex2 for the two complexes: the molecular structures of **[Fe_2^S]**$\cdot 0.5CH_3CN \cdot 0.75Et_2O$ was solved by charge flipping methods and refined on F^2 by full matrix least-squares techniques using SHELXL package.[50] For **[Fe_2^O]** we decided not to refine the solvents using a mask procedure and cctbx to refine instead of SHELXL; it has sense from a physical point of view since there are solvent channels inside the crystal and a dynamical disorder inside them preventing the solvents molecules to be set properly. All non-hydrogen atoms were refined anisotropically for the three complexes. All hydrogen atoms were set geometrically and constrained to ride on their carrier atoms.

Raman spectroscopy.

Raman spectra at 632.8 nm (12 mW at source, Cobolt Lasers, typically 0.15 mW at sample) using an Olympus BX51 uptight microscope and 50x long working distance objective. The excitation light was passed through a polarizing beam splitter and the power controlled by have wave plate and second polarizing beam splitter. The light was directed into the optical

path using a dichroic filter and the Raman scattering collected through a long pass filter to reject the Rayleigh line. The Raman scattering was focused into a multicore fibre (100 micron, round to line arrangement and feed into a Shamrock163 spectrograph with an effect slit of ca. 70 microns onto an idus-416 CCD camera (Andortechnology) Data were recorded using Solis (Andor Technology) with spectral calibration performed using the Raman spectrum of polystyrene.[51] Spectral analysis was carried out using the program Spectragryph.[52]

Mössbauer spectroscopy. ^{57}Fe Mössbauer spectra were recorded with a ^{57}Co source in a Rh matrix using an alternating constant acceleration *Wissel* Mössbauer spectrometer operated in the transmission mode and equipped with a *Janis* closed-cycle helium cryostat. Isomer shifts are given relative to iron metal at ambient temperature. Simulation of the experimental data was performed with the *Mfit* program using *Lorentzian* line doublets: E. Bill, Max-Planck Institute for Chemical Energy Conversion, Mülheim/Ruhr, Germany.

Electrochemistry. Electrochemical experiments were performed in CH_3CN solution under an argon-saturated atmosphere (in a glove box with less than 5 ppm of O_2). The supporting electrolyte tetrabutylammonium perchlorate (Bu_4NClO_4) was used as received and stored in glove box. Cyclic voltammetry and controlled potential electrolysis experiments were carried out by using a PGSTAT100N Metrohm-Autolab potentiostat/galvanostat. A standard three-electrode electrochemical cell was used. Potentials were referred to an Ag/0.01 M $AgNO_3$ reference electrode in CH_3CN + 0.1 M Bu_4NClO_4 and measured potentials were calibrated through the use of an internal Fc/Fc^+ standard. The working electrode was a vitreous carbon disk (3 mm in diameter) polished with 2 μm diamond paste (Mecaprex Presi) for cyclic voltammetry ($E_{p,a}$, anodic peak potential; E_{pc}, cathodic peak potential; $E_{1/2} = (E_{pa} + E_{pc})/2$; $\Delta Ep = E_{pa} - E_{pc}$). Exhaustive electrolysis was carried out on reticulated vitreous carbon electrode 45 PPI (the electrosynthesis Co. Inc.; 1 cm^3). The auxiliary electrode was a Pt wire in CH_3CN + 0.1 M Bu_4NClO_4.

Computational details. All calculations were performed using previously described methods[53-54] using density functional theory as implemented in the ORCA and Gaussian-09 program packages.[55-56] We investigated the oxygen activation by dinuclear **[Fe_2^S]**. Some calculations used a simplified model (starting from the previously described structural properties of **[Mn_2^{SH}]**$^+$)[33] that has all phenyl substituents replaced by methyl; model 1, while

the full system is model 2. A detailed study at the B3LYP level of theory for Model 1 has been performed and covers a range of different electronic and spin states for several complexes. No major differences in structure and relative energies between models 1 and 2 are obtained though. We employed two different unrestricted density functional methods, namely UBLYP[57-58] and UB3LYP[58-59] for geometry optimizations and frequencies: all geometries were fully minimized without constraints in antiferromagnetic spin states. Initial geometry optimizations and frequencies were performed with a double-ζ quality LANL2DZ basis set on Fe (with core potential) and 6-31G* on the rest of the atoms: basis set BS1.[60-61] Energies were improved by single point calculations utilizing a triple-ζ quality LACV3P+ basis set on Fe (with core potential) and 6-311+G* on the rest of the atoms: basis set BS2. Finally, a single point calculation with a polarized continuum model included with a dielectric constant mimicking acetonitrile was done at the BLYP/BS2 level of theory.[62] Raman and vibrational frequencies were calculated in Gaussian-09 from an analytical frequency calculation and unscaled values are reported here unless otherwise mentioned.

Acknowledgements

The authors gratefully acknowledge research support of this work by the China Scholarship Council (LW), the French National Agency for Research in the framework of the "Investissements d'avenir" program (ANR-15-IDEX-02), the Labex ARCANE, the CBH-EUR-GS (ANR-17-EURE-0003) and the ANR-DFG (ANR-16-CE92_0012_01), and the Deutsche Forschungsgemeinschaft (DFG Me1313/14-1, NiFeMim), the COST Action CM1305 (EcostBio) especially via the STSM 34962, The Netherlands Ministry of Education, Culture and Science (Gravity Program 024.001.035 to W.R.B.), and the allocation of beam time for the experiment at the ID23-1 beamline at the European Synchrotron Radiation Facility – ESRF, Grenoble. FGCR thanks the Conacyt Mexico for a studentship.

References

1. Jasniewski, A. J.; Que, L., Dioxygen Activation by Nonheme Diiron Enzymes: Diverse Dioxygen Adducts, High-Valent Intermediates, and Related Model Complexes. *Chem. Rev.* **2018,** *118*, 2554-2592.
2. Solomon, E. I.; Goudarzi, S.; Sutherlin, K. D., O2 Activation by Non-Heme Iron Enzymes. *Biochemistry* **2016,** *55*, 6363-6374.
3. Sahu, S.; Goldberg, D. P., Activation of Dioxygen by Iron and Manganese Complexes: A Heme and Nonheme Perspective. *J. Am. Chem. Soc.* **2016,** *138*, 11410-11428.

4. Guo, M.; Corona, T.; Ray, K.; Nam, W., Heme and Nonheme High-Valent Iron and Manganese Oxo Cores in Biological and Abiological Oxidation Reactions. *ACS Cent. Sci.* **2019,** *5*, 13-28.
5. Gamba, I.; Codola, Z.; Lloret-Fillol, J.; Costas, M., Making and breaking of the O-O bond at iron complexes. *Coord. Chem. Rev.* **2017,** *334*, 2-24.
6. Guengerich, F. P., Mechanisms of Cytochrome P450-Catalyzed Oxidations. *ACS Catal.* **2018,** *8*, 10964-10976.
7. Groves, J. T., Enzymatic C-H bond activation Using push to get pull. *Nat. Chem.* **2014,** *6*, 89-91.
8. Knowles, R. G.; Moncada, S., Nitric oxide synthases in mammals. *Biochem. J.* **1994,** *298*, 249-58.
9. de Visser, S. P., Elucidating enzyme mechanism and intrinsic chemical properties of short-lived intermediates in the catalytic cycles of cysteine dioxygenase and taurine/α-ketoglutarate dioxygenase. *Coord. Chem. Rev.* **2009,** *253*, 754-768.
10. McCoy, J. G.; Bailey, L. J.; Bitto, E.; Bingman, C. A.; Aceti, D. J.; Fox, B. G.; Phillips, G. N., Jr., Structure and mechanism of mouse cysteine dioxygenase. *Proc. Natl. Acad. Sci. U. S. A.* **2006,** *103*, 3084-3089.
11. Stipanuk, M. H., Sulfur amino acid metabolism: Pathways for production and removal of homocysteine and cysteine. *Annu. Rev. Nutr.* **2004,** *24*, 539-577.
12. Straganz, G. D.; Nidetzky, B., Variations of the 2-His-1-carboxylate theme in mononuclear non-heme FeII oxygenases. *ChemBioChem* **2006,** *7*, 1536-1548.
13. Joseph, C. A.; Maroney, M. J., Cysteine dioxygenase: structure and mechanism. *Chem. Commun.* **2007**, 3338-3349.
14. Buongiorno, D.; Straganz, G. D., Structure and function of atypically coordinated enzymatic mononuclear non-heme-Fe(II) centers. *Coord. Chem. Rev.* **2013,** *257*, 541-563.
15. Tchesnokov, E. P.; Fellner, M.; Siakkou, E.; Kleffmann, T.; Martin, L. W.; Aloi, S.; Lamont, I. L.; Wilbanks, S. M.; Jameson, G. N. L., The Cysteine Dioxygenase Homologue from Pseudomonas aeruginosa Is a 3-Mercaptopropionate Dioxygenase. *J. Biol. Chem.* **2015,** *290*, 24424-24437.
16. Roach, P. L.; Clifton, I. J.; Fulop, V.; Harlos, K.; Barton, G. J.; Hajdu, J.; Andersson, I.; Schofield, C. J.; Baldwin, J. E., Crystal structure of isopenicillin N synthase is the first from a new structural family of enzymes. *Nature* **1995,** *375*, 700-4.
17. McQuilken, A. C.; Goldberg, D. P., Sulfur oxygenation in biomimetic non-heme iron–thiolate complexes. *Dalton Trans.* **2012,** *41*, 10883-10899.
18. Gordon, J. B.; McGale, J. P.; Prendergast, J. R.; Shirani-Sarmazeh, Z.; Siegler, M. A.; Jameson, G. N. L.; Goldberg, D. P., Structures, spectroscopic properties, and dioxygen reactivity of 5- and 6-coordinate nonheme iron(II) complexes: A combined enzyme/model study of thiol dioxygenases. *J. Am. Chem. Soc.* **2018,** *140*, 14807-14822.
19. McQuilken, A. C.; Jiang, Y.; Siegler, M. A.; Goldberg, D. P., Addition of Dioxygen to an N4S(thiolate) Iron(II) Cysteine Dioxygenase Model Gives a Structurally Characterized Sulfinato-Iron(II) Complex. *J. Am. Chem. Soc.* **2012,** *134*, 8758-8761.
20. Jiang, Y.; Widger, L. R.; Kasper, G. D.; Siegler, M. A.; Goldberg, D. P., Iron(II)-Thiolate S-Oxygenation by O2: Synthetic Models of Cysteine Dioxygenase. *J. Am. Chem. Soc.* **2010,** *132*, 12214-12215.
21. Sallmann, M.; Siewert, I.; Fohlmeister, L.; Limberg, C.; Knispel, C., A Trispyrazolylborato Iron Cysteinato Complex as a Functional Model for the Cysteine Dioxygenase. *Angew. Chem., Int. Ed.* **2012,** *51*, 2234-2237, S2234/1-S2234/8.

22. Sallmann, M.; Limberg, C., Utilizing the Trispyrazolyl Borate Ligand for the Mimicking of O2-Activating Mononuclear Nonheme Iron Enzymes. *Acc. Chem. Res.* **2015,** *48*, 2734-2743.
23. Sellmann, D.; Shaban, S. Y.; Heinemann, F. W., Transition metal complexes with sulfur ligands. 166: Syntheses, structures and reactivity of electron-rich Fe and Ru complexes with the new pentadentate ligand Et2NpyS4H2 {4-(diethylamino)-2,6-bis[(2-mercaptophenyl)thiomethyl]pyridine}. *Eur. J. Inorg. Chem.* **2004**, 4591-4601.
24. Fiedler, A. T.; Halfen, H. L.; Halfen, J. A.; Brunold, T. C., Synthesis, Structure Determination, and Spectroscopic/Computational Characterization of a Series of Fe(II) Thiolate Model Complexes: Implications for Fe-S Bonding in Superoxide Reductases. *J. Am. Chem. Soc.* **2005,** *127*, 1675-1689.
25. Campanali, A. A.; Kwiecien, T. D.; Hryhorczuk, L.; Kodanko, J. J., Oxidation of Glutathione by [FeIV(O)(N4Py)]2+: Characterization of an [FeIII(SG)(N4Py)]2+ Intermediate. *Inorg. Chem.* **2010,** *49*, 4759-4761.
26. Grapperhaus, C. A.; O'Toole, M. G.; Mashuta, M. S., Synthesis and structure of the tetradeca-iron(III) oxide-alkoxide cluster [Bu4N]2[Fe14O8(OCH2CH3)20Cl8]. *Inorg. Chem. Commun.* **2006,** *9*, 1204-1206.
27. Badiei, Y. M.; Siegler, M. A.; Goldberg, D. P., O2 Activation by Bis(imino)pyridine Iron(II)-Thiolate Complexes. *J. Am. Chem. Soc.* **2011,** *133*, 1274-1277.
28. Musie, G.; Lai, C.-H.; Reibenspies, J. H.; Sumner, L. W.; Darensbourg, M. Y., Pentacoordinate (μ-oxo)diiron(III) thiolate complexes and dimeric iron(II) precursors. *Inorg. Chem.* **1998,** *37*, 4086-4093.
29. Theisen, R. M.; Shearer, J.; Kaminsky, W.; Kovacs, J. A., Steric and Electronic Control over the Reactivity of a Thiolate-Ligated Fe(II) Complex with Dioxygen and Superoxide: Reversible μ-Oxo Dimer Formation. *Inorg. Chem.* **2004,** *43*, 7682-7690.
30. Ohta, S.; Yokozawa, S.; Ohki, Y.; Tatsumi, K., Oxido-Bridged Di-, Tri-, and Tetra-Nuclear Iron Complexes Bearing Bis(trimethylsilyl)amide and Thiolate Ligands. *Inorg. Chem.* **2012,** *51*, 2645-2651.
31. Wang, L.; Gennari, M.; Cantu Reinhard, F. G.; Gutierrez, J.; Morozan, A.; Philouze, C.; Demeshko, S.; Artero, V.; Meyer, F.; de Visser, S. P.; Duboc, C., A Non-Heme Diiron Complex for (Electro)catalytic Reduction of Dioxygen: Tuning the Selectivity through Electron Delivery. *J. Am. Chem. Soc.* **2019,** *141*, 8244-8253.
32. Wang, L. K.; Reinhard, F. G. C.; Philouze, C.; Demeshko, S.; de Visser, S. P.; Meyer, F.; Gennari, M.; Duboc, C., Solvent- and Halide-Induced (Inter)conversion between Iron(II)-Disulfide and Iron(III)-Thiolate Complexes. *Chem. Eur. J.* **2018,** *24*, 11973-11982.
33. Brazzolotto, D.; Cantú Reinhard, F. G.; Smith-Jones, J.; Retegan, M.; Amidani, L.; Faponle, A. S.; Ray, K.; Philouze, C.; de Visser, S. P.; Gennari, M.; Duboc, C., A High-Valent Non-Heme μ-Oxo Manganese(IV) Dimer Generated from a Thiolate-Bound Manganese(II) Complex and Dioxygen. *Angew. Chem. Int. Ed.* **2017,** *56*, 8211-8215.
34. Gennari, M.; Brazzolotto, D.; Pecaut, J.; Cherrier, M. V.; Pollock, C. J.; DeBeer, S.; Retegan, M.; Pantazis, D. A.; Neese, F.; Rouzieres, M.; Clerac, R.; Duboc, C., Dioxygen Activation and Catalytic Reduction to Hydrogen Peroxide by a Thiolate-Bridged Dimanganese(II) Complex with a Pendant Thiol. *J. Am. Chem. Soc.* **2015,** *137*, 8644-8653.
35. Kopf, M. A.; Varech, D.; Tuchagues, J. P.; Mansuy, D.; Artaud, I., New intermediate-spin chloroiron(III) complex with a mixed nitrogen-sulfur co-ordination. *J. Chem. Soc. Dalton Trans.* **1998**, 991-998.
36. Wang, L.; Gennari, M.; Cantú Reinhard, F. G.; Gutiérrez, J.; Morozan, A.; Philouze, C.; Demeshko, S.; Artero, V.; Meyer, F.; de Visser, S. P.; Duboc, C., A Non-Heme Diiron

Complex for (Electro)catalytic Reduction of Dioxygen: Tuning the Selectivity through Electron Delivery. *Journal of the American Chemical Society* **2019,** *141*, 8244-8253.
37. Addison, A. W.; Rao, T. N.; Reedijk, J.; Vanrijn, J.; Verschoor, G. C., SYNTHESIS, STRUCTURE, AND SPECTROSCOPIC PROPERTIES OF COPPER(II) COMPOUNDS CONTAINING NITROGEN SULFUR DONOR LIGANDS - THE CRYSTAL AND MOLECULAR-STRUCTURE OF AQUA 1,7-BIS(N-METHYLBENZIMIDAZOL-2'-YL)-2,6-DITHIAHEPTANE COPPER(II) PERCHLORATE. *J. Chem. Soc. Dalton Trans.* **1984**, 1349-1356.
38. Villar-Acevedo, G.; Lugo-Mas, P.; Blakely, M. N.; Rees, J. A.; Ganas, A. S.; Hanada, E. M.; Kaminsky, W.; Kovacs, J. A., Metal-Assisted Oxo Atom Addition to an Fe(III) Thiolate. *J. Am. Chem. Soc.* **2017,** *139*, 119-129.
39. Zhou, A.; Crossland, P. M.; Draksharapu, A.; Jasniewski, A. J.; Kleespies, S. T.; Que, L., Oxoiron(IV) complexes as synthons for the assembly of heterobimetallic centers such as the Fe/Mn active site of Class Ic ribonucleotide reductases. *J. Biol. Inorg. Chem.* **2018,** *23*, 155-165.
40. Chin, D.-H.; La Mar, G. N.; Balch, A. L., Mechanism of autoxidation of iron(II) porphyrins. Detection of a peroxo-bridged iron(III) porphyrin dimer and the mechanism of its thermal decomposition to the oxo-bridged iron(III) porphyrin dimer. *J. Am. Chem. Soc.* **1980,** *102*, 4344-4350.
41. Zhang, X.; Furutachi, H.; Fujinami, S.; Nagatomo, S.; Maeda, Y.; Watanabe, Y.; Kitagawa, T.; Suzuki, M., Structural and Spectroscopic Characterization of (μ-Hydroxo or μ-Oxo)(μ-peroxo)diiron(III) Complexes: Models for Peroxo Intermediates of Non-Heme Diiron Proteins. *J. Am. Chem. Soc.* **2005,** *127*, 826-827.
42. Dong, Y.; Yan, S.; Young Jr., V. G.; Que Jr., L., Crystal Structure Analysis of a Synthetic Non-Heme Diiron O2 Adduct: Insight into the Mechanism of Oxygen Activation. *Angew. Chem. Int. Ed.* **1996,** *35*, 618-620.
43. Ookubo, T.; Sugimoto, H.; Nagayama, T.; Masuda, H.; Sato, T.; Tanaka, K.; Maeda, Y.; Ōkawa, H.; Hayashi, Y.; Uehara, A.; Suzuki, M., cis-μ-1,2-Peroxo Diiron Complex: Structure and Reversible Oxygenation. *J. Am. Chem. Soc.* **1996,** *118*, 701-702.
44. Coggins, M. K.; Martin-Diaconescu, V.; DeBeer, S.; Kovacs, J. A., Correlation Between Structural, Spectroscopic, and Reactivity Properties Within a Series of Structurally Analogous Metastable Manganese(III), Alkylperoxo Complexes. *J. Am. Chem. Soc.* **2013,** *135*, 4260-4272.
45. Kryatov, S. V.; Rybak-Akimova, E. V.; Schindler, S., Kinetics and Mechanisms of Formation and Reactivity of Non-heme Iron Oxygen Intermediates. *Chem. Rev.* **2005,** *105*, 2175-2226.
46. Ray, K.; Pfaff, F. F.; Wang, B.; Nam, W., Status of Reactive Non-Heme Metal-Oxygen Intermediates in Chemical and Enzymatic Reactions. *J. Am. Chem. Soc.* **2014,** *136*, 13942-13958.
47. Johnson, E. J.; Kleinlein, C.; Musgrave, R. A.; Betley, T. A., Diiron oxo reactivity in a weak-field environment. *Chem. Sci.* **2019,** *10*, 6304-6310.
48. Nurizzo, D.; Mairs, T.; Guijarro, M.; Rey, V.; Meyer, J.; Fajardo, P.; Chavanne, J.; Biasci, J.-C.; McSweeney, S.; Mitchell, E., The ID23-1 structural biology beamline at the ESRF. *J. Synchroton Rad.* **2006,** *13*, 227-238.
49. Kabsch, W., XDS. *Acta Cryst. D* **2010,** *66*, 125-132.
50. Sheldrick, G. M. SHELXTL-Plus, Structure Determination Software Programs, (Version 6.14.), Bruker Analytical X-ray Instruments Inc., Madison, Wisconsin, USA, 1998.
51. McCreery, R. L., *Raman Spectroscopy for Chemical Analysis*. Ch. 10, John Wiley & Sons, Inc.: New York, 2000.

52. http://spectragryph.com.
53. Cantú Reinhard, F. G.; Faponle, A. S.; de Visser, S. P., Substrate Sulfoxidation by an Iron(IV)-Oxo Complex: Benchmarking Computationally Calculated Barrier Heights to Experiment. *J. Phys. Chem. A* **2016,** *120*, 9805-9814.
54. Cantú Reinhard, F. G.; Sainna, M. A.; Upadhyay, P.; Balan, G. A.; Kumar, D.; Fornarini, S.; Crestoni, M. E.; de Visser, S. P., A Systematic Account on Aromatic Hydroxylation by a Cytochrome P450 Model Compound I: A Low-Pressure Mass Spectrometry and Computational Study. *Chem. Eur. J.* **2016,** *22*, 18608-18619.
55. Neese, F., The ORCA program system. *Wiley Interdiscip. Rev. Comput. Mol. Sci.* **2012,** *2*, 73-78.
56. Gaussian 09, R. D., *M. J. Frisch, G. W. Trucks, H. B. Schlegel, G. E. Scuseria, M. A. Robb, J. R. Cheeseman, G. Scalmani, V. Barone, B. Mennucci, G. A. Petersson, H. Nakatsuji, M. Caricato, X. Li, H. P. Hratchian, A. F. Izmaylov, J. Bloino, G. Zheng, J. L. Sonnenberg, M. Hada, M. Ehara, K. Toyota, R. Fukuda, J. Hasegawa, M. Ishida, T. Nakajima, Y. Honda, O. Kitao, H. Nakai, T. Vreven, J. A. Montgomery, Jr., J. E. Peralta, F. Ogliaro, M. Bearpark, J. J. Heyd, E. Brothers, K. N. Kudin, V. N. Staroverov, R. Kobayashi, J. Normand, K. Raghavachari, A. Rendell, J. C. Burant, S. S. Iyengar, J. Tomasi, M. Cossi, N. Rega, J. M. Millam, M. Klene, J. E. Knox, J. B. Cross, V. Bakken, C. Adamo, J. Jaramillo, R. Gomperts, R. E. Stratmann, O. Yazyev, A. J. Austin, R. Cammi, C. Pomelli, J. W. Ochterski, R. L. Martin, K. Morokuma, V. G. Zakrzewski, G. A. Voth, P. Salvador, J. J. Dannenberg, S. Dapprich, A. D. Daniels, Ö. Farkas, J. B. Foresman, J. V. Ortiz, J. Cioslowski, and D. J. Fox, Gaussian, Inc., Wallingford CT, 2009.*
57. Becke, A. D., DENSITY-FUNCTIONAL EXCHANGE-ENERGY APPROXIMATION WITH CORRECT ASYMPTOTIC-BEHAVIOR. *Phys. Rev. A* **1988,** *38*, 3098-3100.
58. Lee, C. T.; Yang, W. T.; Parr, R. G., DEVELOPMENT OF THE COLLE-SALVETTI CORRELATION-ENERGY FORMULA INTO A FUNCTIONAL OF THE ELECTRON-DENSITY. *Phys. Rev. B* **1988,** *37*, 785-789.
59. Becke, A. D., A NEW MIXING OF HARTREE-FOCK AND LOCAL DENSITY-FUNCTIONAL THEORIES. *J. Chem. Phys.* **1993,** *98*, 1372-1377.
60. Hay, P. J.; Wadt, W. R., ABINITIO EFFECTIVE CORE POTENTIALS FOR MOLECULAR CALCULATIONS - POTENTIALS FOR THE TRANSITION-METAL ATOMS SC TO HG. *J. Chem. Phys.* **1985,** *82*, 270-283.
61. Hehre, W. J.; Ditchfield, R.; Pople, J. A., *J. Chem. Phys.* **1972,** *56*, 2257–2262.
62. Tomasi, J.; Mennucci, B.; Cammi, R., Quantum Mechanical Continuum Solvation Models. *Chem. Rev.* **2005,** *105*, 2999-3094.